

This Dissertation  
entitled  
SEARCH FOR GAUGE-MEDIATED SUPERSYMMETRY BREAKING  
typeset with NDdiss2 $\epsilon$  v3.2013 (2013/04/16) on February 6, 2018 for  
Allison Reinsvold Hall

This L<sup>A</sup>T<sub>E</sub>X 2 $\epsilon$  classfile conforms to the University of Notre Dame style guidelines as of Fall 2012. However it is still possible to generate a non-conformant document if the instructions in the class file documentation are not followed!

Be sure to refer to the published Graduate School guidelines at <http://graduateschool.nd.edu> as well. Those guidelines override everything mentioned about formatting in the documentation for this NDdiss2 $\epsilon$  class file.

It is YOUR responsibility to ensure that the Chapter titles and Table caption titles are put in CAPS LETTERS. This classfile does *NOT* do that!

*This page can be disabled by specifying the “noinfo” option to the class invocation. (i.e., \documentclass[... ,noinfo]{nddiss2e} )*

**This page is *NOT* part of the dissertation/thesis. It should be disabled before making final, formal submission, but should be included in the version submitted for format check.**

NDdiss2 $\epsilon$  documentation can be found at these locations:

<http://www.gsu.nd.edu>  
<http://graduateschool.nd.edu>

# SEARCH FOR GAUGE-MEDIATED SUPERSYMMETRY BREAKING

A Dissertation

Submitted to the Graduate School  
of the University of Notre Dame  
in Partial Fulfillment of the Requirements  
for the Degree of

Doctor of Philosophy

by

Allison Reinsvold Hall

---

Michael Hildreth, Director

Graduate Program in Physics

Notre Dame, Indiana

February 2018

This is the abstract.

# CONTENTS

FIGURES . . . . .	iv
TABLES . . . . .	v
CHAPTER 1: INTRODUCTION . . . . .	1
CHAPTER 2: Theoretical Motivation . . . . .	2
2.1 The Standard Model of particle physics . . . . .	2
2.2 Supersymmetry . . . . .	2
2.3 Gauge-mediated supersymmetry breaking . . . . .	2
CHAPTER 3: The Large Hadron Collider . . . . .	3
3.1 Introduction . . . . .	3
3.2 Injector Chain . . . . .	3
3.3 Vacuum and magnet system . . . . .	3
3.4 Operating parameters . . . . .	3
CHAPTER 4: CMS DETECTOR . . . . .	4
4.1 Coordinate system . . . . .	4
4.2 Superconducting solenoid . . . . .	5
4.3 Tracker . . . . .	6
4.3.1 Pixel detector . . . . .	6
4.3.2 Strip detectors . . . . .	7
4.3.3 Tracker performance . . . . .	7
4.4 Electromagnetic Calorimeter (ECAL) . . . . .	7
4.5 Hadron calorimeter (HCAL) . . . . .	7
4.6 Muon system . . . . .	8
CHAPTER 5: Event Reconstruction in the CMS Detector . . . . .	9
5.0.1 Particle Flow Algorithm . . . . .	9
5.0.2 Jet reconstruction . . . . .	9
5.0.3 Pileup subtraction . . . . .	9

CHAPTER 6: TRIGGER SYSTEM . . . . .	10
6.1 Overview of CMS trigger system . . . . .	10
6.1.1 Level 1 Trigger . . . . .	10
6.1.2 High Level Trigger . . . . .	11
6.2 Analysis triggers . . . . .	11
6.3 Trigger efficiency . . . . .	11
6.3.1 Efficiency of di-electron control sample . . . . .	12
CHAPTER 7: Sample Selection . . . . .	13
7.1 Object Selection . . . . .	13
7.1.1 Photon identification . . . . .	13
7.1.2 Electron identification . . . . .	13
7.1.3 Fake identification . . . . .	13
7.1.4 Object Cleaning . . . . .	14
7.1.5 Lepton veto . . . . .	15
7.1.6 Signal region and control samples . . . . .	15
CHAPTER 8: DATA ANALYSIS AND BACKGROUND ESTIMATION METH-	
ODS . . . . .	16
8.1 Overview . . . . .	16
8.2 QCD background . . . . .	17
8.2.1 Di-EM $p_T$ reweighting . . . . .	17
8.2.2 Cross check on QCD background . . . . .	19
8.2.3 Systematic uncertainties on the QCD background . . . . .	22
8.3 Electroweak background . . . . .	22
8.3.1 Fake rate calculation . . . . .	24
8.3.2 Calculating EWK estimate . . . . .	24
8.3.3 Composition of $e\gamma$ sample . . . . .	24
8.3.4 EWK results . . . . .	25
8.4 Irreducible background . . . . .	25
8.4.1 Cross checking normalization . . . . .	26
CHAPTER 9: Results and Interpretations . . . . .	27
9.1 Prediction versus observation . . . . .	27
9.2 Simplified Models . . . . .	28
9.3 Signal acceptance and efficiency . . . . .	29
9.4 Limits . . . . .	29
CHAPTER 10: Conclusions . . . . .	30
BIBLIOGRAPHY . . . . .	31

## FIGURES

4.1	Schematic of the CMS detector. . . . .	5
4.2	Schematic of the CMS tracker system. Detector modules are represented by single lines, and back-to-back modules are represented by double lines. . . . .	7
8.1	The di-EM $p_T$ vector, shown in light blue, is the vector sum of the $p_T$ of the two photons in the event, shown in blue. The magnitude of the di-EM $p_T$ vector is used to model the hadronic recoil, shown in red. .	18
8.2	Di-EM $p_T$ distributions of the $ff$ control sample (black) and the $\gamma\gamma$ candidate sample (red). The ratio plot on the bottom shows the $\gamma\gamma/ff$ ratios that are used to reweight the $ff$ $E_T^{\text{miss}}$ distribution. . . . .	19
8.3	Di-EM $p_T$ distributions of the $ff$ control sample (black) and the $\gamma\gamma$ candidate sample (red). The ratio plot on the bottom shows the $\gamma\gamma/ff$ ratios that are used to reweight the $ff$ $E_T^{\text{miss}}$ distribution. . . . .	20
8.4	Di-EM $p_T$ distributions of the $ff$ control sample (black) and the $\gamma\gamma$ candidate sample (red). The ratio plot on the bottom shows the $\gamma\gamma/ff$ ratios that are used to reweight the $ff$ $E_T^{\text{miss}}$ distribution. . . . .	21
8.5	Di-EM $p_T$ distributions of the $ff$ control sample (black) and the $\gamma\gamma$ candidate sample (red). The ratio plot on the bottom shows the $\gamma\gamma/ff$ ratios that are used to reweight the $ff$ $E_T^{\text{miss}}$ distribution. . . . .	22
8.6	The ratio of $\gamma\gamma$ to $ff$ events for $E_T^{\text{miss}} < 100$ GeV. The ratio has been fit to a constant function, which can then be used to extrapolate to the $E_T^{\text{miss}} > 100$ GeV signal region. This provides an alternative estimation method for the QCD background. . . . .	23
8.7	Data versus Monte Carlo comparison of the $e\gamma$ control sample $E_T^{\text{miss}}$ distribution. To determine the relative contributions of the $\gamma + \text{jet}$ and $W\gamma$ processes, the data distribution was fit using the $\gamma + \text{jet}$ and $W\gamma$ shapes as templates. The data are shown in black, and the total MC prediction is shown in blue. The $\gamma + \text{jet}$ MC (red) was scaled to 80% of the observed events in data. and the $W\gamma$ MC (green) was scaled to 20% of the data distribution. . . . .	25

9.1	Diagrams showing the production of signal events in the collision of two protons with four momenta $P_1$ and $P_2$ . In gluino $\tilde{g}$ pair production in the T5gg simplified model (left), the gluino decays to an antiquark $\bar{q}$ , quark $q$ , and neutralino $\tilde{\chi}_1^0$ . In squark $\tilde{q}$ pair production in the T6gg simplified model (right), the squark decays to a quark and a neutralino. In both cases, the neutralino subsequently decays to a photon $\gamma$ and a gravitino $\tilde{G}$ . In the diagram on the right, we do not distinguish between squarks and antisquarks. . . . .	28
-----	---	----

## TABLES

7.1	ELECTROMAGNETIC OBJECT DEFINITIONS . . . . .	14
7.2	EFFECTIVE AREAS FOR ISOLATION CORRECTIONS . . . . .	15
8.1	COMPARISON BETWEEN REWEIGHTING METHOD AND RA- TIO METHOD FOR THE QCD BACKGROUND ESTIMATE . . .	24
9.1	EXPECTED AND OBSERVED EVENTS IN THE SIGNAL REGION	27



## CHAPTER 1

### INTRODUCTION

The Large Hadron Collider (LHC) at the European Organization for Nuclear Research (CERN) is the largest machine in the world and an incredible feat of engineering and science. This machine is used to study elementary particles and their interactions. At the LHC, proton-proton collisions occur at center-of-mass energies up to 13 TeV.

The Standard Model of particle physics describes fundamental particles and their interactions to an incredible level of precision. This is described in more detail in Chapter XX.

The CMS detector and various subsystems will be described in Chapter 4. Finally, Chapter XX will include a discussion of the results of this analysis and suggestions for future work.

Introduction

Chapter 1: Theory Motivation Standard Model Why we need BSM SUSY GMSB  
Chapter 2: LHC About CERN How the accelerator works Chapter 3: CMS Detector

Chapter 4: Object Reconstruction

Chapter 5: Trigger

Chapter 6: Event Selection Including object cleaning

## CHAPTER 2

### Theoretical Motivation

2.1 The Standard Model of particle physics

2.2 Supersymmetry

2.3 Gauge-mediated supersymmetry breaking

## CHAPTER 3

### The Large Hadron Collider

#### 3.1 Introduction

The Large Hadron Collider is a particle accelerator located at CERN, the European Organization for Nuclear Research.

#### 3.2 Injector Chain

#### 3.3 Vacuum and magnet system

#### 3.4 Operating parameters

## CHAPTER 4

### CMS DETECTOR

The Compact Muon Solenoid (CMS) detector is a multi-purpose detector designed to accurately measure the energy of all particles produced in proton-proton collisions. Figure 8.7 shows a schematic of the detector as a whole. Each subdetector will be described in more detail in the following sections. Moving radially outward from the interaction point, the subdetectors are the silicon pixel and strip tracker (Section 4.3), the electromagnetic calorimeter (Section 4.4), the hadron calorimeter (Section 4.5), and the muon system (Section 4.6). For a full description of the CMS detector, see [6]. The full length of the CMS detector is 21.6 m, the diameter of the detector is 21.6 m, and the total weight is 12500 t.

#### 4.1 Coordinate system

The origin of the CMS detector coordinate system is located at the nominal collision point. The  $z$ -axis is oriented along the beam direction, with the positive  $z$ -axis pointing in the counter-clockwise direction when viewing the LHC from above. The  $y$ -axis points vertically upward, and the  $x$ -axis points toward the center of the LHC. The  $xy$ -plane is referred to as the transverse plane.

Due to the nature of particle collisions, however, Cartesian coordinates are often not the most convenient. Because protons are not elementary particles, it is actually the individual quarks or gluons within the proton that interact during the collision. This means that the collision will not be at rest in the lab frame, but will have some

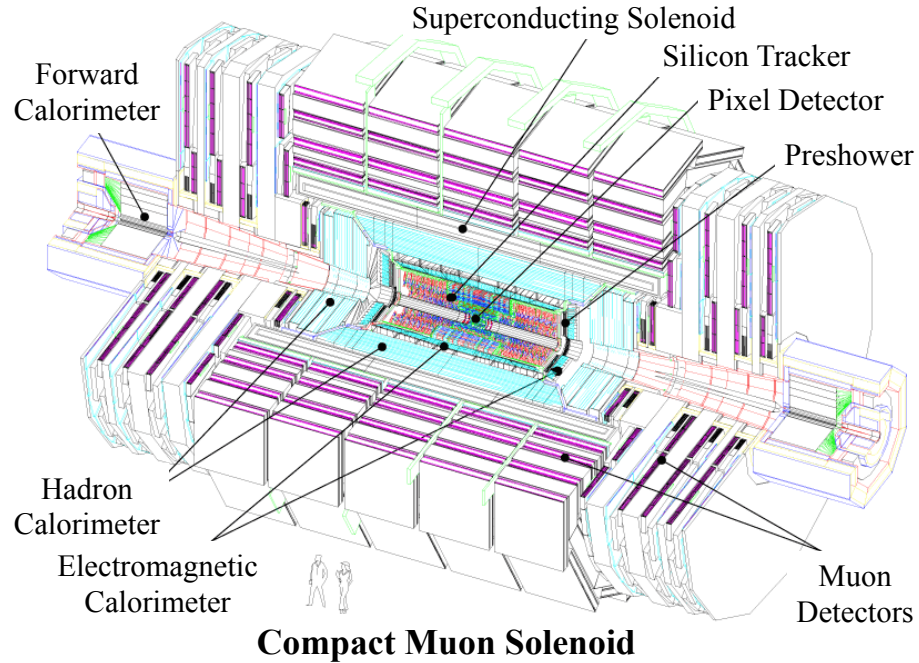


Figure 4.1. Schematic of the CMS detector.

non-zero velocity along the  $z$ -axis. To deal with this, it is beneficial to use coordinates that are invariant under boosts in the  $z$  direction. CMS follows the particle physics convention of describing the position of a particle in terms of its transverse momentum, azimuthal angle, and pseudorapidity. The transverse momentum  $p_T$  is defined as the magnitude of the momentum in the  $xy$  plane. The azimuthal angle  $\phi$  is defined in the transverse plane, with  $\phi = 0$  corresponding to the positive  $x$ -axis. Finally, the pseudorapidity is defined as  $\eta = -\ln \tan(\theta/2)$ , where the polar angle  $\theta$  is measured from the  $z$ -axis.

## 4.2 Superconducting solenoid

One of the most important components of the CMS detector is the superconducting solenoid. The solenoid provides the bending power necessary to precisely measure the momentum of all charged particles produced in the collision. The mag-

net is located between the calorimeters and the muon system. It is 13 m long and has an inner diameter of 6 m. It is capable of producing magnetic fields up to 4 T, although the magnet is generally operated at 3.8 T to prolong its lifetime. At full current, the magnet has a stored energy of 2.6 GJ. A 10,000 ton iron yoke made up of 5 wheels in the barrel and 6 endcap disks serves to return the magnetic flux. A detailed description of the CMS magnet can be found in [7].

### 4.3 Tracker

The innermost subdetector is the silicon tracker [8, 9]. The overall dimensions of the tracker are 5.6 m long and 1.2 m in radius. The full tracking system is cylindrical in shape and is comprised of a barrel and two endcaps, each of which is split into layers of silicon pixel detectors and layers of silicon micro-strip detectors. In total, there are 66 million  $150 \times 100 \mu\text{m}$  pixels and 9.6 million strips that are between 80 and  $180 \mu\text{m}$  wide. Figure 4.2 shows a schematic drawing of the layout of the tracker subsystems.

#### 4.3.1 Pixel detector

Due to the high occupancy of the tracker within 10 cm of the beam pipe, pixel detectors rather than strip detectors are used as the innermost layers of the tracker. Three barrel layers and two disks of pixel detectors in the endcap give three high-precision points for every charged particle moving away from the interaction point. The small pixel size of  $150 \times 100 \mu\text{m}$  is critical to allow for good secondary vertex reconstruction and for forming seed tracks that are used for high level triggering (see Chapter 6) and for the reconstruction of charged particles in the event (see Chapter 5). The three barrel layers are 53 cm long and are located at mean radii of 4.4, 7.3 and 10.2 cm. The endcap modules extend radially from 6 to 15 cm in radius and are placed on each side at  $z = \pm 34.5$  and  $z = \pm 46.5$  cm. The endcaps extend

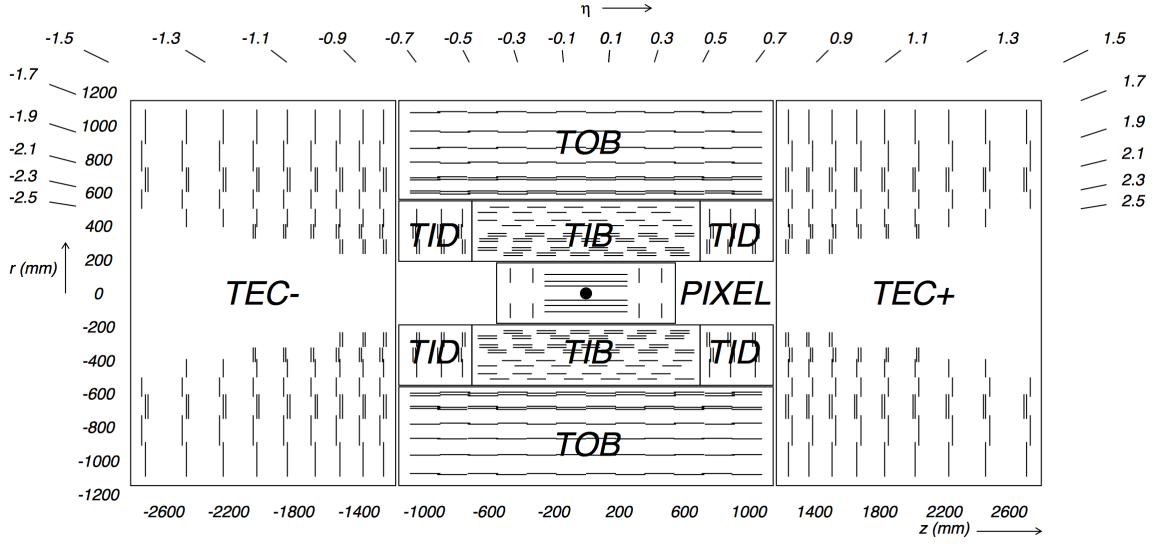


Figure 4.2. Schematic of the CMS tracker system. Detector modules are represented by single lines, and back-to-back modules are represented by double lines.

the coverage of the subdetector out to  $|\eta| < 2.5$ .

#### 4.3.2 Strip detectors

#### 4.3.3 Tracker performance

For charged hadrons with transverse momentum  $p_T$  less than 20 GeV, the  $p_T$  can be measured with a resolution of 1%.

### 4.4 Electromagnetic Calorimeter (ECAL)

Very important. Finds photons.

### 4.5 Hadron calorimeter (HCAL)

brass sampling calorimeter

## 4.6 Muon system

The muon subsystem is located outside of the solenoid and is embedded in the return yoke for the magnetic flux. Three different types of detectors are used in the muon system: drift tube chambers (DTC) = positively charged wire within gas volume. Muon knocks electrons off atoms in the gas, which are attracted to the wire. Can determine where electrons hit and where the muon was from the wire to get 2 coordinates for its position. Barrel Cathode strip chamber (CSC) = better for high flux areas. Crisscrossing positive and negative wires. Muons knock off electrons, which go to positive wires. Ions move toward negative wires. Two position coordinates. Endcaps.



## CHAPTER 5

### Event Reconstruction in the CMS Detector

5.0.1 Particle Flow Algorithm

5.0.2 Jet reconstruction

5.0.3 Pileup subtraction

## CHAPTER 6

### TRIGGER SYSTEM

#### 6.1 Overview of CMS trigger system

Many more collisions occur within the LHC than can be written out to tape and stored for future analysis. At the four interaction points, including inside the CMS detector, bunches of protons collide every 25 ns. For every bunch crossing, there are on average 25 “soft-scatter” collisions (XX Look up this number XX). This corresponds to an overall event rate of XX. Given that each event produces approximately 1 MB of data, it is impossible to store every event or even the majority of events. This has been especially true in recent years, with the LHC continually breaking new records for instantaneous luminosity.

To solve this problem, the CMS detector includes a sophisticated trigger system to determine which events make it into the XX% that gets written to tape and eventually analyzed. The CMS trigger system is divided into two steps: the Level 1 (L1) trigger which uses customized hardware located in the detector cavern, and the software-based High Level Trigger (HLT). The L1 trigger reduces the rate from 1 GHz to approximately 100 kHz, and the HLT makes the final decisions necessary to reduce the rate to 1 kHz, the maximum amount that can be written to tape and stored. Both steps of the CMS trigger are described in more detail below.

##### 6.1.1 Level 1 Trigger

The L1 trigger reduces the rate from 1 GHz to 100 kHz.

### 6.1.2 High Level Trigger

## 6.2 Analysis triggers

## 6.3 Trigger efficiency

An important input to the analysis is the overall trigger efficiency. Due to the similarity of the ECAL response to electrons and photons, the trigger efficiency can be calculated from  $Z \rightarrow ee$  events in data using the tag-and-probe method (CITE XX). In this method, two electron candidates are required. One serves as the “tag” and has to pass electron identification criteria. The second electron candidate serves as the “probe” and has to satisfy the same selection criteria as our offline photon identification requirements (see Section ??). In order to ensure a high purity of electromagnetic objects, the invariant mass of the di-electron system must be between 75 and 105 GeV.

### Control trigger

The efficiency of the HLT path or trigger filter that is being studied is given by the following equation, where  $N_{total}$  is the total number of tag-and-probe pairs passing all requirements, and  $N_{pass}$  is the number of tag-and-probe pairs in which the probe passes the trigger filter.

$$\epsilon_{trig} = N_{pass}/N_{total} \quad (6.1)$$

Because our analysis trigger is seeded by the OR of multiple SingleEG and DoubleEG L1 seeds, the names of which changed over the course of the 2016 data-taking period, calculating the L1 efficiency on its own proved tricky. Instead, it was simpler to calculate the total efficiency with which photon candidates pass both the L1 seed and the leading leg of the HLT path. This efficiency as a function of photon  $p_T$  is shown in Figure ??. The efficiency was fit to an error function to calculate the overall efficiency at the plateau. For photon  $p_T > 40$  GeV, the leading filter is XX% efficient.

XX Insert figure XX

Tag and probe objects for the trailing leg efficiency must pass the same set of requirements as those used in the leading leg efficiency calculation, with the additional requirement that the tag must pass the leading filter. This requirement comes from how HLT paths are run. Filters are processed sequentially, and if an event fails one filter, the subsequent filters are skipped. Figure ?? shows the efficiency of the trailing filter as a function of photon  $p_T$ .

XX Insert figure XX

Finally, we calculated the efficiency of the trigger with respect to the diphoton invariant mass. For this calculation, we required two photons passing our analysis selection criteria and the trailing leg of the trigger and one photon passing the leading leg of the trigger. The efficiency was given by the number of diphoton events passing the full HLT path over the total number of diphoton events passing our requirements. The efficiency of the trigger as a function of invariant mass is shown in Figure ??.

XX Insert figure XX

### 6.3.1 Efficiency of di-electron control sample

One of the important control samples for our analysis is made up of  $Z \rightarrow ee$  events. Due to the invariant mass requirement on the primary analysis, however, a second trigger was used to collect events for the di-electron control sample. This trigger shares all of the same requirements as the primary trigger, with two exceptions: the invariant mass of the two electromagnetic objects is required to be greater than 55 GeV rather than 95 GeV, and both electromagnetic objects are required to be matched to a pixel seed. The pixel seed match requirement affects the efficiency of the trailing leg of the control trigger. This efficiency is shown in Figure ??.

XX Insert figure XX

## CHAPTER 7

### Sample Selection

#### 7.1 Object Selection

In addition to photons and electrons, a third, orthogonal object definition referred to as “fake” photons is also used. Fakes are primarily electromagnetically-rich jets that have been misidentified as photons. As will be described in Chapter 8, a control sample made up of events with two fakes is used to estimate the QCD background.

##### 7.1.1 Photon identification

##### 7.1.2 Electron identification

##### 7.1.3 Fake identification

Electromagnetically-rich jets that have been misidentified as photons make up the majority of the objects that satisfy our “fake” definition. These objects are taken from a photon ID sideband. Fakes must pass all of the photon identification criteria described in Section 7.1.1, except they are required to fail either the  $\sigma_{i\eta i\eta}$  or the charged hadron isolation requirement. This is described in detail in Table 7.2 (XX better if column widths the same XX)

STOLEN The uncorrected isolation variables are PF objects Pt sums in a cone 0.3 around the photon and also subjected to the photon footprint removal using the association map of the PF objects. The charge hadron Isolation is calculated using the PF objects that their tracks are associated with the primary vertex only, thus removing pile-up charge hadrons. STOLEN

TABLE 7.1

## ELECTROMAGNETIC OBJECT DEFINITIONS

ID Requirement	Photons	Electrons	Fakes
Pixel seed veto	Applied	Reversed	Applied
$\sigma_{i\eta i\eta}$	$< 0.01022$		$0.01022 < \sigma_{i\eta i\eta} < 0.015$
Charged hadron isolation	$< 0.441$		$0.441 < iso < 15$
Photon isolation	$< 2.571 + 0.0047 p_T$		
Neutral hadron isolation	$< 2.2725 + 0.0148 p_T + 0.000017 p_T^2$		
R9	$> 0.5$		
H/E	$< 0.0396$		

Definitions of photon, electron, and fakes used to define the signal and control samples for this analysis. “Fakes” refer to jets that have been misidentified as photons. The definitions of each of the variables used in the object ID’s can be found in Section ??.

## 7.1.4 Object Cleaning

In order to avoid double counting particles, a set of object cleaning rules are applied. First, because muons are reconstructed with a higher purity than any other particle, any electromagnetic object (photon, electron, or fake) that is within  $\Delta R < 0.3$  of a muon candidate is removed. Second, any photon that overlaps within  $\Delta R < 0.3$  of an electron is removed. Finally, if a fake overlaps with an electron or photon candidate within  $\Delta R < 0.4$ , the fake candidate is removed. The larger  $\Delta R$  separation for fakes is due to the fact that fakes are primarily jets. As described in Section XX, jets are reconstructed using the anti- $p_T$  algorithm with a distance parameter of 0.4.

TABLE 7.2

EFFECTIVE AREAS FOR ISOLATION CORRECTIONS

$ \eta $ Range	Photon Iso	Neutral Hadron Iso	Charged Hadron Iso
$ \eta  < 1.0$	0.120	0.0597	0.0360
$1.0 <  \eta  < 1.479$	0.1107	0.0807	0.0377

Effective areas used in the definition of photon, charged hadron, and neutral hadron isolation values.

#### 7.1.5 Lepton veto

In addition to the cuts described above, any event that contains additional muons or electrons is vetoed. No additional leptons are present in the SUSY signals of interest, so applying a lepton veto will not hurt our signal sensitivity. More importantly, by vetoing on the presence of additional leptons, our analysis becomes orthogonal to other CMS searches for gauge-mediated supersymmetry breaking with photons in the final state. As described in Section XX, this is particularly important for the combination paper.

#### 7.1.6 Signal region and control samples

ff, ee, gg, eg, good times.

## CHAPTER 8

### DATA ANALYSIS AND BACKGROUND ESTIMATION METHODS

#### 8.1 Overview

There are several Standard Model processes that can mimic our signal events. The largest background contribution comes from quantum chromodynamics (QCD) processes. These are primarily multi-jet events, where electromagnetically-rich jets are misidentified as photons, but can also include processes with true photons either from associated photon production or initial-state radiation. In both cases, there is no inherent  $E_T^{\text{miss}}$  in the event. Instead, the measured  $E_T^{\text{miss}}$  is actually the result of mismeasured hadronic activity. As described in Section 8.2, this background is estimated in an entirely data-driven way using a control region derived from a sideband of our photon ID.

The second-largest background is the electroweak (EWK) background. This background is comprised of  $W\gamma$  or  $W+\text{jet}$  events where  $W \rightarrow e\nu$ . In this case, there is inherent  $E_T^{\text{miss}}$  from the neutrino, and these events can mimic our signal topology if the electron is misidentified as a photon. By measuring the misidentification rate in data, we can use an  $e\gamma$  control sample to estimate the contribution from the EWK background. The EWK background estimation method is described in detail in Section 8.3.

Finally, there is an irreducible background from  $Z\gamma\gamma \rightarrow \nu\nu\gamma\gamma$  events. This background is modeled via simulation and is described in Section 8.4.



## 8.2 QCD background

Due to the large QCD cross section, the most significant background for this analysis comes from QCD events without true  $E_T^{\text{miss}}$  and without two real photons. The observed  $E_T^{\text{miss}}$  is the result of mismeasured hadronic activity, and in most cases the “photons” are misidentified jets with a large electromagnetic component.

To estimate the contribution from the QCD background in our signal region, we use the “fake” object selection that was described in Section 7.1. The fake identification criteria is orthogonal to the nominal photon identification, and therefore provides a sideband that can be used as a control region. The  $E_T^{\text{miss}}$  tail of the QCD background is modeled using a “fake-fake” (“ $ff$ ”) control sample made up of events with two fakes that pass the additional criteria outlined in Section 7.1.6.

### 8.2.1 Di-EM $p_T$ reweighting

Because the  $E_T^{\text{miss}}$  in the QCD background and the  $ff$  control sample arises from poorly measured hadronic activity, it is important that the amount of hadronic activity in the control sample matches that of the  $\gamma\gamma$  events we are trying to model.

To account for potential differences between the samples, we define a variable referred to as the “di-EM  $p_T$ ” of an event. Di-EM  $p_T$  is defined as the magnitude of the vector sum of the transverse momentum of the two electromagnetic objects (photons, electrons or fakes):

$$\vec{p}_T^{\text{di-EM}} = \vec{p}_{T1} + \vec{p}_{T2} \quad (8.1)$$

As illustrated in Figure 8.1, the di-EM  $p_T$  variable is used as a measure of the total hadronic recoil. Because CMS measures the energies of electromagnetic objects with greater precision than the energy of jets, this variable is a more accurate representation of the hadronic recoil than simply adding up the transverse momentum of

the jets themselves.

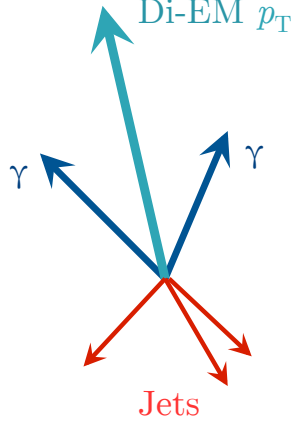


Figure 8.1: The di-EM  $p_T$  vector, shown in light blue, is the vector sum of the  $p_T$  of the two photons in the event, shown in blue. The magnitude of the di-EM  $p_T$  vector is used to model the hadronic recoil, shown in red.

The di-EM  $p_T$  distributions for the  $\gamma\gamma$  candidate sample and the  $ff$  control sample are shown in Figure 8.2. The  $ff$  events are the reweighted using the  $\gamma\gamma/ff$  ratios displayed in the ratio plot of Figure 8.2. The  $ff$   $E_T^{\text{miss}}$  distribution is normalized to the  $E_T^{\text{miss}} < 50$  GeV region of the  $\gamma\gamma$  sample, where signal contamination is minimal.

The unweighted  $ff$  and  $\gamma\gamma$   $E_T^{\text{miss}}$  distributions are shown in Figure 8.3. A comparison between the unweighted and di-EM  $p_T$  reweighted  $ff$   $E_T^{\text{miss}}$  distributions is shown in Figure 8.4. Finally, Figure 8.5 compares the reweighted  $ff$   $E_T^{\text{miss}}$  distribution to the candidate  $\gamma\gamma$   $E_T^{\text{miss}}$  distribution.

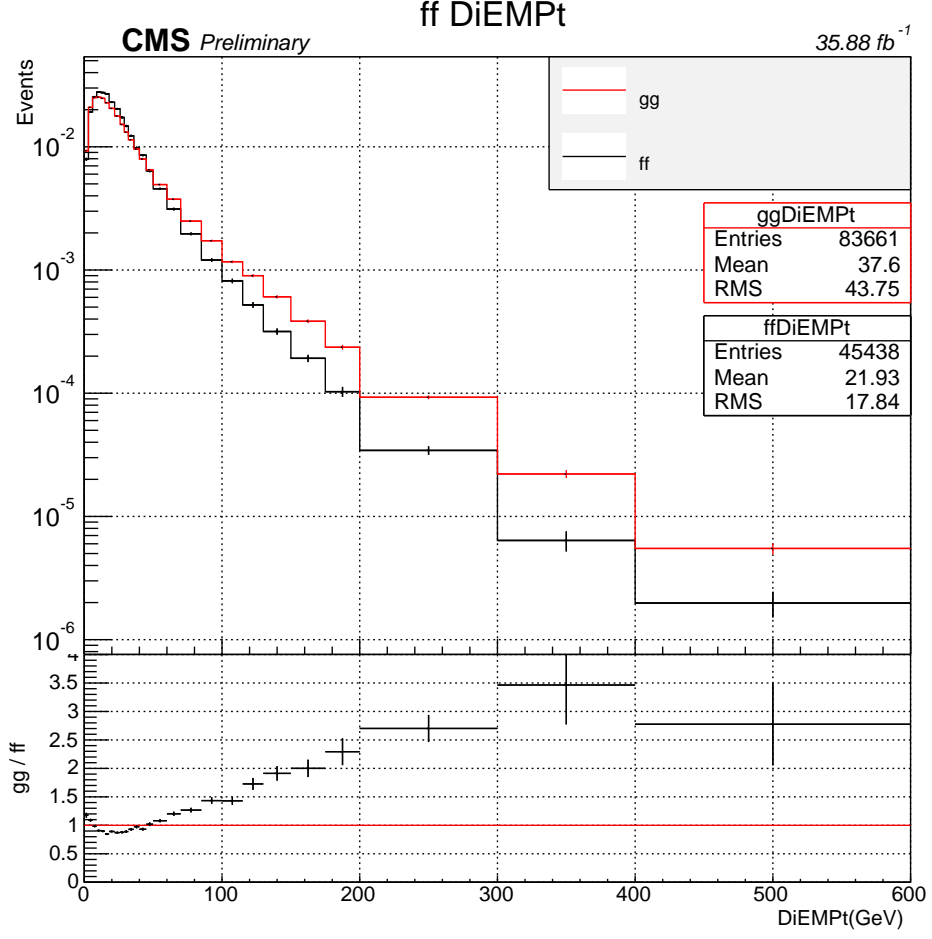


Figure 8.2: Di-EM  $p_T$  distributions of the  $ff$  control sample (black) and the  $\gamma\gamma$  candidate sample (red). The ratio plot on the bottom shows the  $\gamma\gamma/ff$  ratios that are used to reweight the  $ff$   $E_T^{\text{miss}}$  distribution.

### 8.2.2 Cross check on QCD background

In order to set a systematic uncertainty on the overall  $E_T^{\text{miss}}$  shape predicted using the di-EM  $p_T$  reweighting method, we sought an alternate way to estimate the QCD background. This cross check relies on the assumption that the ratio of  $\gamma\gamma$  events to  $ff$  events should not depend sensitively on  $E_T^{\text{miss}}$ . If this assumption is true, then we should be able to extrapolate from the low- $E_T^{\text{miss}}$  control region to the high- $E_T^{\text{miss}}$  signal region.

Figure 8.6 shows the ratio of  $\gamma\gamma/ff$  as a function of  $E_T^{\text{miss}}$  in the  $E_T^{\text{miss}} < 100$  GeV

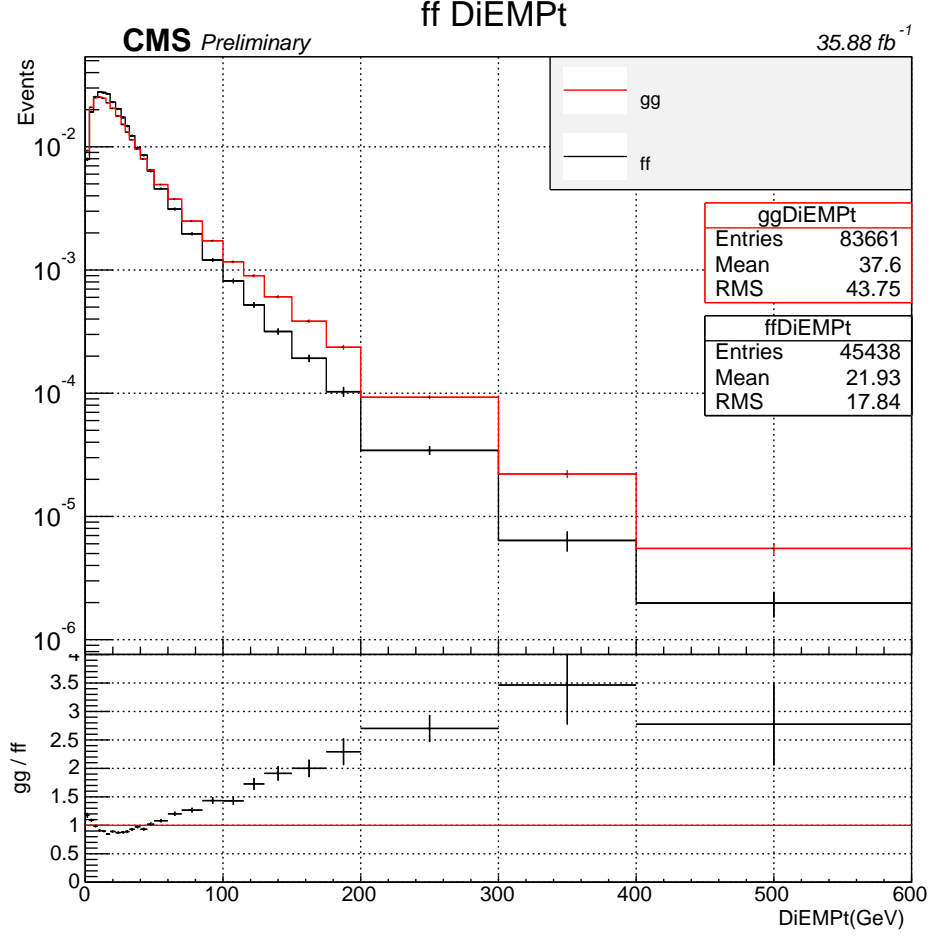


Figure 8.3: Di-EM  $p_T$  distributions of the  $ff$  control sample (black) and the  $\gamma\gamma$  candidate sample (red). The ratio plot on the bottom shows the  $\gamma\gamma/ff$  ratios that are used to reweight the  $ff$   $E_T^{\text{miss}}$  distribution.

control region. The ratio has been fit to a constant function  $f(E_T^{\text{miss}})$ . Using this function, the expected number of  $\gamma\gamma$  events in bin  $i$  of the signal region is given by the following equation:

$$N_{\gamma\gamma}^i = f(E_T^{\text{miss}}) \times N_{ff}^i \quad (8.2)$$

Table 8.1 compares the expected QCD background contribution as predicted with the cross check method to that predicted with the di-EM  $p_T$  reweighting method. For the cross check method, the uncertainty arising from the choice of fitting function is

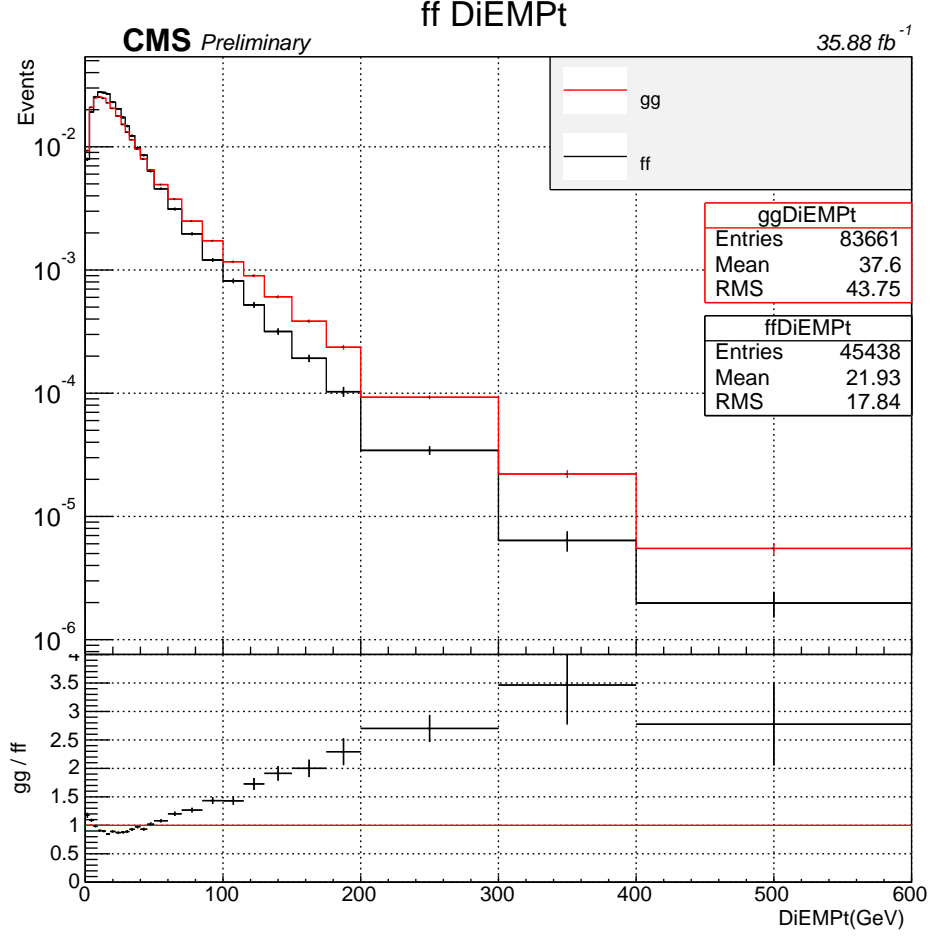


Figure 8.4: Di-EM  $p_T$  distributions of the  $ff$  control sample (black) and the  $\gamma\gamma$  candidate sample (red). The ratio plot on the bottom shows the  $\gamma\gamma/ff$  ratios that are used to reweight the  $ff$   $E_T^{\text{miss}}$  distribution.

estimated by taking the difference between the results when fitting to a constant to the results when fitting to a linear function. In addition, the cross check uncertainties listed in Table 8.1 include the statistical uncertainty from the limited control sample statistics and the  $1\sigma$  uncertainties from the fit. For the di-EM  $p_T$  reweighting method, the uncertainties include the statistical uncertainty and the uncertainty from the di-EM  $p_T$  reweighting procedure (this systematic is described in detail in Section 8.2.3).

The two methods give overlapping predictions within uncertainty, and therefore

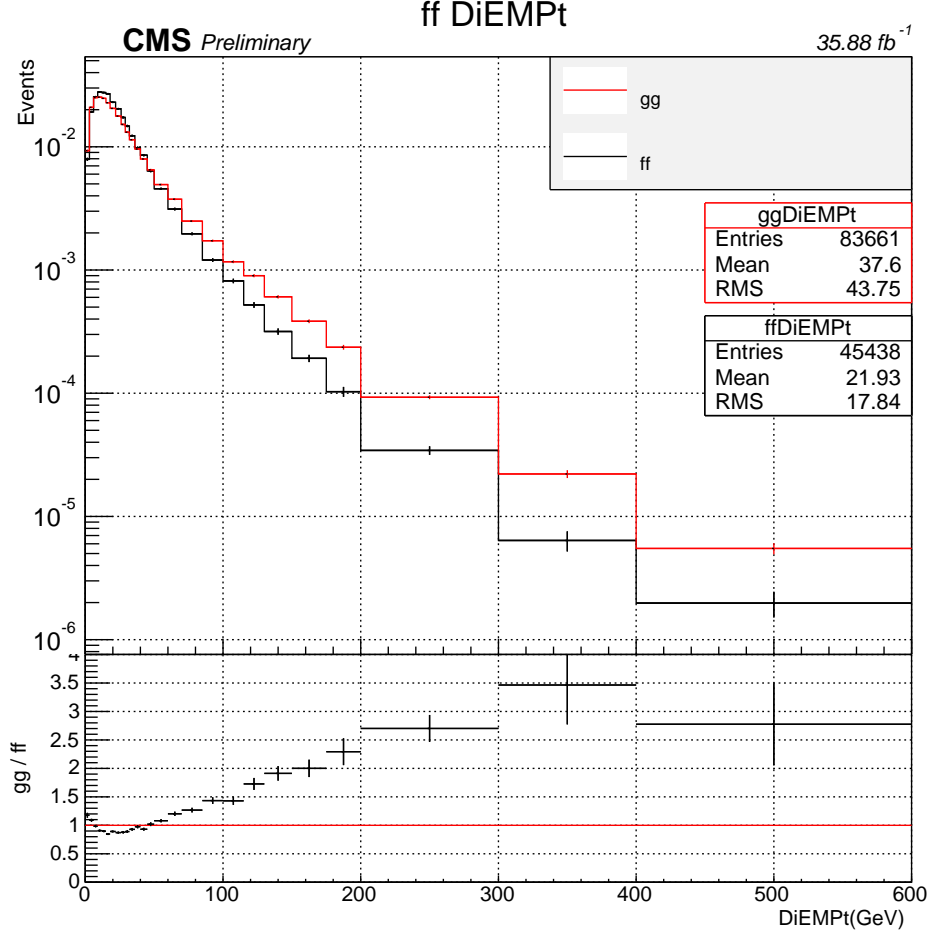


Figure 8.5: Di-EM  $p_T$  distributions of the  $ff$  control sample (black) and the  $\gamma\gamma$  candidate sample (red). The ratio plot on the bottom shows the  $\gamma\gamma/ff$  ratios that are used to reweight the  $ff$   $E_T^{\text{miss}}$  distribution.

this cross check serves to validate our di-EM  $p_T$  reweighting background estimation method. The difference between the two methods is taken as a systematic uncertainty on the overall  $E_T^{\text{miss}}$  shape.

### 8.2.3 Systematic uncertainties on the QCD background

## 8.3 Electroweak background

The subdominant background for this search is comprised of  $W\gamma$  and  $W+\text{jet}$  events where  $W \rightarrow e\nu$  and the electron is misidentified as a photon. This background

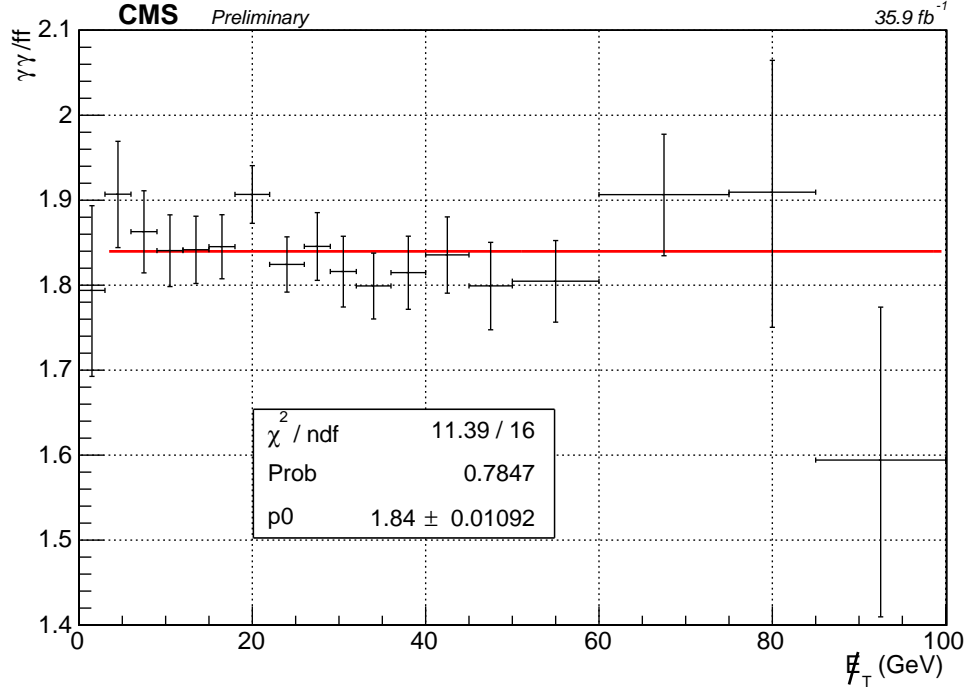


Figure 8.6: The ratio of  $\gamma\gamma$  to  $ff$  events for  $E_T^{\text{miss}} < 100$  GeV. The ratio has been fit to a constant function, which can then be used to extrapolate to the  $E_T^{\text{miss}} > 100$  GeV signal region. This provides an alternative estimation method for the QCD background.

is referred to as the electroweak (EWK) background. Unlike the QCD background, there is inherent  $E_T^{\text{miss}}$  in these events from the escaping neutrino.

To estimate this background, we first calculate the rate at which electrons are misidentified as photons. This is done by comparing the invariant mass peak in a double electron sample with the invariant mass peak in a sample of events with one electron and one photon. The calculation of this "fake rate" is described in detail in Section 8.3.1. To get the final expected contribution from the EWK background in our signal region, the fake rate is used to calculate a transfer factor. By applying the transfer factor to an  $e\gamma$  control sample, we are able to estimate how many of our candidate  $\gamma\gamma$  events are actually events with one photon and one electron that has been misidentified as a photon.

TABLE 8.1

COMPARISON BETWEEN REWEIGHTING METHOD AND RATIO  
METHOD FOR THE QCD BACKGROUND ESTIMATE

$E_T^{\text{miss}}$ bin (Gev)	Reweighted ff estimate	Ratio method estimate
100 – 115	$69.23^{+15.18}_{-12.68}$	$55.19^{+12.03}_{-10.33}$
115 – 130	$30.89^{+11.76}_{-8.82}$	$22.08^{+8.39}_{-6.59}$
130 – 150	$25.98^{+11.95}_{-8.61}$	$16.55^{+7.56}_{-5.69}$
150 – 185	$20.49^{+10.12}_{-7.11}$	$14.72^{+7.26}_{-5.45}$
185 – 250	$8.74^{+11.65}_{-5.89}$	$3.68^{+4.85}_{-2.47}$
> 250	$5.13^{+11.86}_{-4.43}$	$1.84^{+4.23}_{-1.60}$

Comparison of the background estimate using the di-EM  $p_T$  reweighting method and the  $\gamma\gamma/ff$  ratio method. The uncertainties on the di-EM  $p_T$  reweighting method include the statistical uncertainties and the reweighting uncertainty. The uncertainties on the ratio method include the statistical uncertainties, the uncertainties in the fit parameter, and the uncertainty from the choice of fit function.

### 8.3.1 Fake rate calculation

### 8.3.2 Calculating EWK estimate

### 8.3.3 Composition of $e\gamma$ sample

The  $e\gamma$  control sample is primarily made up of  $\gamma + \text{jets}$  or  $W\gamma$  events. A data versus Monte Carlo comparison of this control sample is shown in Figure ???. The data distribution was fit using the simulated  $\gamma + \text{jet}$  and  $W\gamma$  shapes as templates. From the fit, it was determined that 80% of the  $e\gamma$  events observed in data are from  $\gamma + \text{jets}$  processes, and the remaining 20% are  $W\gamma$  events. In the  $E_T^{\text{miss}} > 100$  GeV signal region, however,  $W\gamma$  events dominate. For  $100 < E_T^{\text{miss}} < 130$  GeV, 12.1% of the MC prediction is made up of  $\gamma$  plus jet processes. For  $E_T^{\text{miss}} > 130$  GeV, however,  $\gamma$  plus jet events contribute only 2.6%.



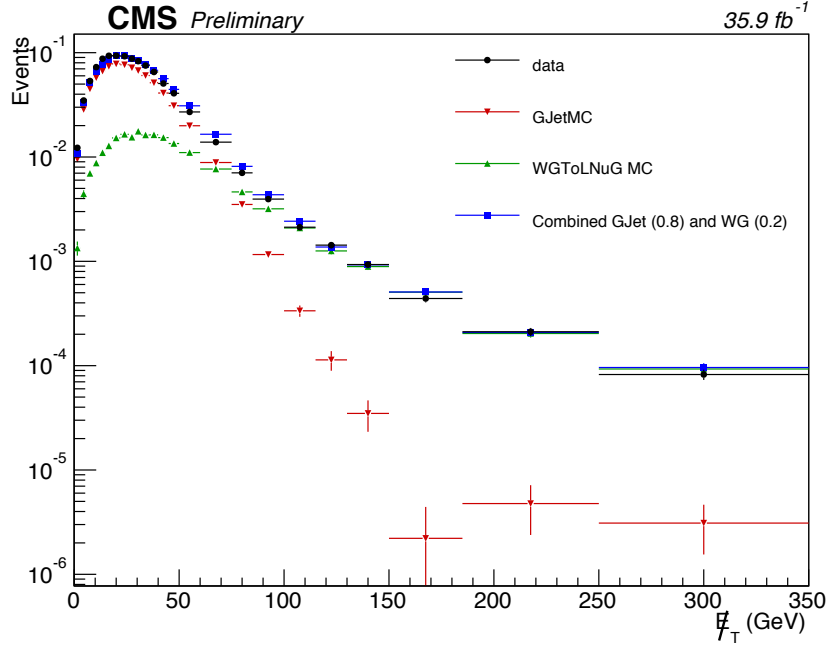


Figure 8.7: Data versus Monte Carlo comparison of the  $e\gamma$  control sample  $E_T^{\text{miss}}$  distribution. To determine the relative contributions of the  $\gamma + \text{jet}$  and  $W\gamma$  processes, the data distribution was fit using the  $\gamma + \text{jet}$  and  $W\gamma$  shapes as templates. The data are shown in black, and the total MC prediction is shown in blue. The  $\gamma + \text{jet}$  MC (red) was scaled to 80% of the observed events in data, and the  $W\gamma$  MC (green) was scaled to 20% of the data distribution.

#### 8.3.4 EWK results

Table XX shows the final EWK estimate in the six signal region bins. There are two sources of uncertainty on the EWK estimate: the statistical uncertainty from the limited number of  $e\gamma$  events observed in data, and the 30% systematic uncertainty from the calculation of the fake rate. Both of these are displayed in Table XX.

#### 8.4 Irreducible background

In addition to the QCD and EWK backgrounds, there is a small irreducible background from  $Z\gamma\gamma \rightarrow \nu\nu\gamma\gamma$  events. Because there is inherent  $E_T^{\text{miss}}$  from this process, it is not included in the QCD background, and because it has two true photons, it

is not included in the EWK background either. We model this background using MC simulation, and assign a 50% uncertainty to the estimate to cover any potential mismodeling.

XX List datasets XX

#### 8.4.1 Cross checking normalization

To cross check the  $Z\gamma\gamma$  normalization obtained from data, we compare the observed number of  $Z\gamma\gamma \rightarrow ee\gamma\gamma$  events seen in data to that predicted via MC. These processes are different only in the decay mode of the  $Z$  boson, and therefore should give an accurate indication of how well the process is simulated in MC. The results are shown in Table XX.

## CHAPTER 9

### Results and Interpretations

#### 9.1 Prediction versus observation

Table 9.1 shows the expected and observed numbers of events for each bin in the signal region.

TABLE 9.1

EXPECTED AND OBSERVED EVENTS IN THE SIGNAL REGION

$E_{\text{T}}^{\text{miss}}$ (GeV)	Exp. QCD	Exp. EWK	$Z\gamma\gamma$ events	Total exp.	Observed
100 – 115	$69.23^{+20.67}_{-18.91}$	$8.17 \pm 2.5$	$1.30 \pm 0.65$	$78.69^{+22.58}_{-20.98}$	65
115 – 130	$30.89^{+14.69}_{-12.46}$	$5.50 \pm 1.70$	$1.14 \pm 0.57$	$37.53^{+16.05}_{-14.04}$	27
130 – 150	$25.98^{+15.21}_{-12.76}$	$4.78 \pm 1.48$	$1.12 \pm 0.56$	$31.88^{+16.44}_{-14.20}$	17
150 – 185	$20.49^{+11.65}_{-9.16}$	$3.95 \pm 1.24$	$1.32 \pm 0.66$	$25.76^{+12.80}_{-10.59}$	13
185 – 250	$8.74^{+12.70}_{-7.765}$	$3.52 \pm 1.11$	$1.28 \pm 0.64$	$13.55^{+13.05}_{-8.31}$	8
$\geq 250$	$5.13^{+12.31}_{-5.514}$	$2.11 \pm 0.69$	$1.14 \pm 0.57$	$8.38^{+12.48}_{-5.88}$	10

## 9.2 Simplified Models

Two simplified models are used in the interpretation of the results. The T5gg simplified model assumes gluino ( $\tilde{g}$ ) pair production and the T6gg model assumes squark ( $\tilde{q}$ ) pair production. Example decay chains for both models are shown in Figure 9.1.

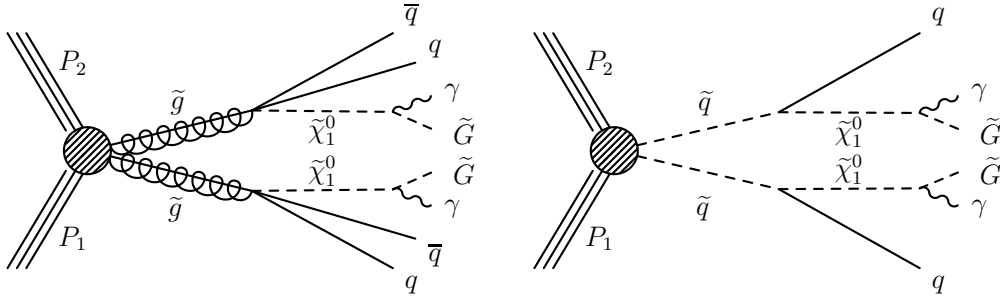


Figure 9.1: Diagrams showing the production of signal events in the collision of two protons with four momenta  $P_1$  and  $P_2$ . In gluino  $\tilde{g}$  pair production in the T5gg simplified model (left), the gluino decays to an antiquark  $\bar{q}$ , quark  $q$ , and neutralino  $\tilde{\chi}_1^0$ . In squark  $\tilde{q}$  pair production in the T6gg simplified model (right), the squark decays to a quark and a neutralino. In both cases, the neutralino subsequently decays to a photon  $\gamma$  and a gravitino  $\tilde{G}$ . In the diagram on the right, we do not distinguish between squarks and antisquarks.

In both models, the lightest supersymmetric particle (LSP) is the gravitino,  $\tilde{G}$ , which is taken to be nearly massless. The next-to-lightest supersymmetric particle (NLSP) is the neutralino,  $\tilde{\chi}_1^0$ . The models assume 100% branching fraction for  $\tilde{\chi}_1^0 \rightarrow \tilde{G}\gamma$  and  $\tilde{g} \rightarrow q\bar{q}\tilde{\chi}_1^0$  and  $\tilde{q} \rightarrow q\tilde{\chi}_1^0$ .

In order to study the expected SUSY signal distributions, two signal Monte Carlo scans were produced. The T5Wg scan was produced in bins of gluino mass and neutralino mass, and the T6Wg scan was produced in bins of squark mass and neu-

tralino mass. The leading-order event generator MADGRAPH5\_aMC@NLO [2] is used to simulate the signal samples, which were generated with either two gluinos or two squarks and up to two additional partons in the matrix element calculation. The parton showering, hadronization, multiple-parton interactions, and the underlying event were described by the PYTHIA 8 [11] program with the CUETP8M1 generator tune. The detector response is simulated using CMS fast simulation [1].

A total of 40,000 events were produced for each bin, except for bins with gluino or squark masses above 2.0 TeV, where only 20,000 events were produced per bin. For gluino masses from 1,400 to 2,500 GeV, events were generated in bins of 50 GeV. In the T6Wg scan, the squark masses ranged from 1,400 GeV to 2,050 GeV in bins of 50 GeV. The neutralino masses ranged from 10 GeV up to the mass of the gluino or squark and were binned in 100 GeV segments. Finer binning was used in the compressed region where  $M_{\tilde{\chi}_1^0}$  is within 300 GeV of  $M_{\tilde{g}}$  or  $M_{\tilde{q}}$ , and in the region with low  $M_{\tilde{\chi}_1^0}$ . These mass ranges were selected to overlap and expand upon the mass ranges excluded by previous searches [? ? ].

The parton distribution functions are obtained from NNPDF3.0 [3] The cross sections are calculated at NLO+NLL accuracy [10, 4], with all the unconsidered sparticles assumed to be heavy and decoupled. The uncertainties on the cross sections are calculated as described in Ref. [5].

### 9.3 Signal acceptance and efficiency

### 9.4 Limits

## CHAPTER 10

### Conclusions

In this dissertation, a search for gauge-mediated supersymmetry breaking in events with two photons and missing transverse momentum was described. The analysis was performed with data taken with the CMS detector in 2016, but suggestions to improve the background estimation methods for the analysis of the 2017 data were also explored. Results were interpreted in the context of two simplified models, one assuming squark pair production and the other assuming gluino pair production. No evidence for gauge-mediated supersymmetry breaking (GMSB) was observed, and limits were placed on the masses of supersymmetric particles. Work is also ongoing to combine this analysis with other analyses targeting photon final states, in order to set limits on more comprehensive GMSB models.

## BIBLIOGRAPHY

1. S. Abdullin, P. Azzi, F. Beaudette, P. Janot, and A. Perrotta. The fast simulation of the CMS detector at LHC. *J. Phys. Conf. Ser.*, 331:032049, 2011. doi: 10.1088/1742-6596/331/3/032049.
2. J. Alwall, R. Frederix, S. Frixione, V. Hirschi, F. Maltoni, O. Mattelaer, H. S. Shao, T. Stelzer, P. Torrielli, and M. Zaro. The automated computation of tree-level and next-to-leading order differential cross sections, and their matching to parton shower simulations. *JHEP*, 07:079, 2014. doi: 10.1007/JHEP07(2014)079.
3. R. D. Ball et al. Parton distributions for the LHC Run II. *JHEP*, 04:040, 2015. doi: 10.1007/JHEP04(2015)040.
4. W. Beenakker, S. Brensing, M. Krämer, A. Kulesza, E. Laenen, and I. Niessen. Soft-gluon resummation for squark and gluino hadroproduction. *JHEP*, 12:041, 2009. doi: 10.1088/1126-6708/2009/12/041.
5. C. Borschensky, M. Krämer, A. Kulesza, M. Mangano, S. Padhi, T. Plehn, and X. Portell. Squark and gluino production cross sections in  $pp$  collisions at  $\sqrt{s} = 13, 14, 33$  and 100 TeV. *Eur. Phys. J. C*, 74:3174, 2014. doi: 10.1140/epjc/s10052-014-3174-y.
6. S. Chatrchyan et al. The CMS experiment at the CERN LHC. *JINST*, 3:S08004, 2008. doi: 10.1088/1748-0221/3/08/S08004.
7. CMS Collaboration. The CMS magnet project: Technical Design Report. CMS Technical proposal CERN-LHCC-97-010, CMS-TDR-1, CERN, 1997. URL <https://cds.cern.ch/record/331056>.
8. CMS Collaboration. The CMS tracker system project: Technical Design Report. CMS Technical proposal CERN-LHCC-98-006, CMS-TDR-5, CERN, 1997. URL <https://cds.cern.ch/record/368412>.
9. CMS Collaboration. The CMS tracker: addendum to the Technical Design Report. CMS Technical proposal CERN-LHCC-2000-016, CMS-TDR-5-add-1, CERN, 2000. URL <https://cds.cern.ch/record/490194>.
10. A. Kulesza and L. Motyka. Soft gluon resummation for the production of gluino-gluino and squark-antisquark pairs at the LHC. *Phys. Rev. D*, 80:095004, 2009. doi: 10.1103/PhysRevD.80.095004.

11. T. Sjöstrand, S. Mrenna, and P. Z. Skands. A brief introduction to PYTHIA 8.1. *Comput. Phys. Commun.*, 178:852, 2008. doi: 10.1016/j.cpc.2008.01.036.

*This document was prepared & typeset with pdfL<sup>A</sup>T<sub>E</sub>X, and formatted with  
NDdiss2<sub>ε</sub> classfile (v3.2013[2013/04/16]) provided by Sameer Vijay and updated  
by Megan Patnott.*